7-1-2007

Analyses of Internal Solitary Waves Generated at the Columbia River Plume Front Using SAR Imagery

Jiayi Pan
Portland State University

David A. Jay
Portland State University

Citation Details

Jiayi, P., Jay, D. A., & Orton, P. M. (2007). Analyses of internal solitary waves generated at the Columbia River plume front using SAR imagery. Journal Of Geophsical Research-Part C-Oceans, 112(7), 1-11.

JOURNAL OF GEOPHYSICAL RESEARCH, VOL. 112, C07014, doi:10.1029/2006JC003688, 2007

Analyses of internal solitary waves generated at the Columbia River plume front using SAR imagery

Jiayi Pan,[1] David A. Jay,[1] and Philip M. Orton[2]

Received 8 May 2006; revised 20 February 2007; accepted 19 March 2007; published 13 July 2007.

[1] Internal solitons generated at the Columbia River plume front during ebb tide are displayed on a synthetic aperture radar (SAR) image taken on 26 July 2004 at 14:24:22 UTC. Scale analyses suggest that these internal solitons belong to the finite-depth category. A theoretical model, relating the radar backscatter cross section to dynamic parameters of internal solitons in the continuous stratification, is developed. Using the model and background stratification data collected by the River Influences on Shelf Ecosystem (RISE) project in July 2004, we extract the soliton dynamic parameters of the half-width, amplitude, phase speed, and average energy flux per crest length along a typical section across the internal solitons. The observed stratification is simulated by using a theoretical model parameterized by pycnocline depth, thickness, and maximum buoyancy frequency. The half-width, amplitude, phase speed, and energy flux of the leading soliton at the section are 119.3 m, 9.3 m, 0.69 m s^{-1}, and 417.4 W m^{-1} with the uncertainty ranges of ±14.7 m, ±2.6 m, ±0.10 m s^{-1}, and ±281.6 W m^{-1}, respectively. Sensitivity analyses reveal that the extraction of the soliton half-width from the SAR image is not affected by the stratification. The amplitude is less influenced by the pycnocline thickness than the depth and is independent of the maximum buoyancy frequency.

Citation: Pan, J., D. A. Jay, and P. M. Orton (2007), Analyses of internal solitary waves generated at the Columbia River plume front using SAR imagery, *J. Geophys. Res.*, *112*, C07014, doi:10.1029/2006JC003688.

1. Introduction

[2] Internal waves are a major dynamic feature in the Columbia River plume area [D. A. Jay et al., Asymmetry of tidal plume fronts in an Eastern Boundary Current regime, submitted to *Journal of Marine Systems*, 2006]. Previous investigators have shown that the internal waves in this area have diverse origins. One category is generated by interaction between shoreward-propagating tides and the sharp topography of the continental slope. *Moum et al.* [2003] made detailed observations of an internal solitary wave train propagating shoreward over the Oregon's continental shelf. In the region, highly nonlinear and shoreward-traveling internal waves were also reported by *Stanton and Ostrovsky* [1998]. Another important kind of internal wave, which we study here, is generated at the river plume front and propagates offshore. *Nash and Moum* [2005] explored the generation mechanism of these internal waves, and *Orton and Jay* [2005] characterized their role in the plume ecosystem. Nash and Moum concluded that wave fission from the decelerating plume front is responsible for the internal wave production. Orton and Jay emphasized the role of plume fronts and waves in mixing plume and ambient water and in causing resuspension of nutrients from the seabed in waters <60 m deep. However, the dynamic features of the internal waves traveling after they depart from the plume front are not well understood. We extract these features here using satellite data and field observations.

[3] Internal waves can be observed from space. A spaceborne synthetic aperture radar (SAR) can detect radar backscatter signals from ocean surface under all weather and light conditions with a spatial resolution as fine as several meters. The velocity field induced by an internal soliton forms a convergence zone on one side of the soliton crest and a divergence on the other. The convergence roughens the sea surface by intensifying surface waves, whereas the divergence smoothes the ocean surface by suppressing the waves [*Osborn and Burch*, 1980]. The rougher surface has a greater radar backscatter section, while the smoother one produces less backscattering. Therefore, on SAR images, one can see bright and dark textures associated with internal waves under the ocean surface.

[4] Using SEASAT SAR images, *Apel and Gonzalez* [1983] detected nonlinear features of a group of internal waves off Baja California, and *Fu and Holt* [1984] found signatures of internal solitary waves in the Gulf of California. With SAR data, *Liu et al.* [1998] observed conversion of an internal soliton from a depression to an elevation wave as lower-layer depth decreased. *Zheng et al.* [2001]

[1]Department of Civil and Environmental Engineering, Portland State University, Portland, Oregon, USA.
[2]Lamont-Doherty Earth Observatory, Columbia University, Palisades, New York, USA.

0148-0227/07/2006JC003688$09.00

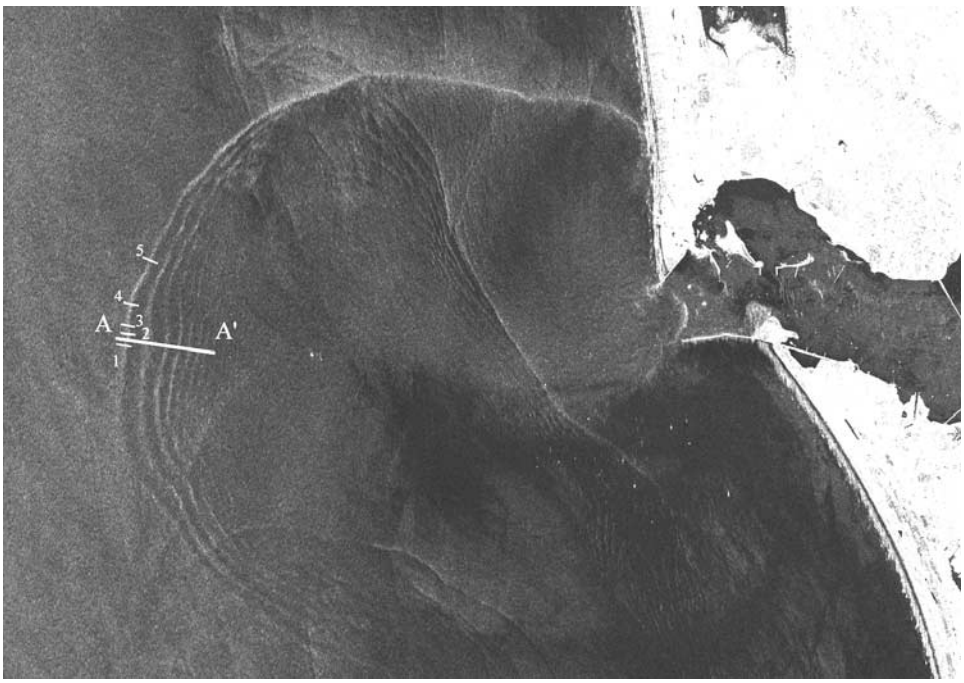

Figure 1. The SAR image taken on 26 July 2004 at 14:24:22 UTC, in which sections AA′, 1, 2, 3, 4, and 5 are illustrated.

developed physical models to determine characteristic half-width of internal solitons using the SAR image. Recently, SAR data were used to detect the Delaware Bay plume fronts and to parameterize the plume dynamic features [*Zheng et al.*, 2004]. All these investigations suggest that SAR observations are important data sources for internal wave studies.

[5] In this study, we use SAR image data together with contemporary cruise data to extract dynamic parameters of internal solitons generated at the Columbia River plume fronts. Specifically, RADARSAT-1 SAR data for July 2004 are used along with density measurements from a RISE project cruise. We obtain the dynamic characteristics of the internal solitons along a typical section on the SAR image. Section 2 describes the satellite SAR image data. Section 3 specifies the dynamics of the internal solitons in finite water depth and radar backscatter cross section per unit area caused by this soliton category. The dynamic parameters are calculated in section 4. Section 5 presents analyses of sensitivity of the method to stratification parameters and uncertainties of the derived parameters. Section 6 summarizes the results.

2. SAR Image Data

[6] RADARSAT-1 is an Earth observation satellite developed by Canadian Space Agency. Launched in November 1995, RADARSAT-1 produces imagery for operational monitoring services on a global basis. It is equipped with a powerful and state-of-the-art SAR instrument, which acquires images of the Earth day and night under all weather conditions. The RADARSAR-1 SAR can be steered to capture data over a 1175-km-wide area using seven beams.

[7] The SAR image used in this study was taken on 26 July 2004 at 14:24:22 UTC in the standard mode. This image was received and processed at the Alaska Satellite Facility in Fairbanks, Alaska. The SAR image (Figure 1) shows a group of internal waves in the Columbia River plume area. Their patterns suggest that these waves were traveling offshore from the plume front, implying that they were generated at the plume front by the mechanism described in the paper of *Nash and Moum* [2005]. The bright strips of the internal waves in the SAR image are displayed in Figure 2, together with the bathymetry,

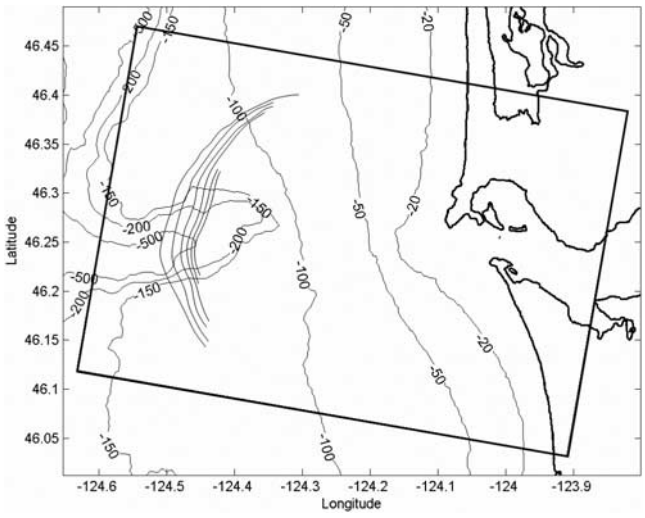

Figure 2. The internal waves with bathymetry contours and the SAR image frame in a rectangle.

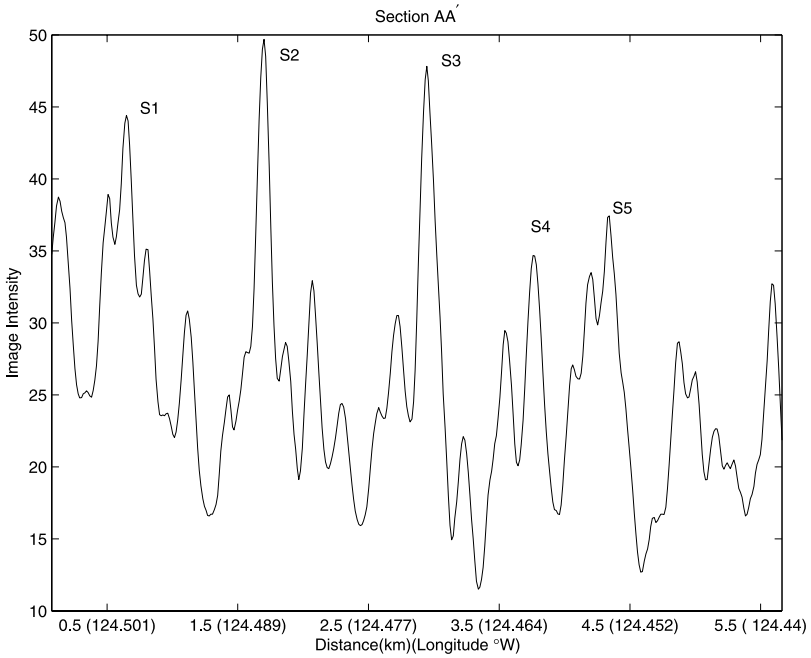

Figure 3. SAR image intensity value versus distance and longitude along section AA′. The solitons are marked by S1, S2, S3, S4, and S5.

coastal line, and SAR image boundary lines. In order to quantify the internal waves, we select a section across the internal waves, which is identified as AA′ in Figure 1. A three-point running mean method is twice applied to the image intensity along this section to suppress noise, and the smoothed image intensity is plotted against position in Figure 3, revealing five internal solitons marked by S1, S2, S3, S4, and S5. On the basis of these image intensity values, we obtained soliton wavelengths, which are defined as distances between contiguous paired-soliton crests (λ_{ij}, where subscript i and j represent two contiguous solitons). The wavelengths and their means are listed in Table 1.

3. SAR Backscatter Cross Section Caused by Finite-Depth Internal Soliton

[8] Two-dimensional internal waves may be described by a stream function ψ. The stream function is a product of linear wave speed and the vertical displacement: $\psi = c_0 I(\xi, z)$, where $\xi = x - ct$; c_0 and c are the linear wave and soliton speeds, respectively. The vertical displacement has a separable form $I(x, z, t) = \eta(\xi)\phi(z)$. The horizontal and vertical velocities are $u = \partial\psi/\partial z$ and $w = -\partial\psi/\partial\xi$, respectively. If we neglect ambient shear, the vertical structure function (ϕ) is a solution of the linear Sturm-Liouville equation [*Apel et al.*, 1985; *Fu and Holt*, 1984] with the normalization $\phi(z_0) = 1$, where z_0 is the depth corresponding to the maximum value of ϕ.

[9] There are three theoretical regimes that describe horizontal behaviors of internal solitons in various circumstances: shallow water [*Benjamin*, 1966; *Benney*, 1966], finite depth [*Joseph*, 1977; *Kubota et al.*, 1978], and deep water [*Benjamin*, 1967; *Ono*, 1975]. The criteria for discriminating the three cases depend on the ratio of the water depth to the soliton horizontal scale [*Liu et al.*, 1985; *Zheng et al.*, 1993; 1995]. For this case, the soliton scale parameters satisfy the finite-depth soliton criteria, suggesting that the solitons in this study belong to the finite-depth category. For the finite-depth internal solitons, the amplitude η satisfies the following equation [*Apel et al.*, 1985; *Joseph*, 1977; *Zheng et al.*, 1993]

$$\frac{\partial\eta}{\partial t} + c_0\frac{\partial\eta}{\partial x} + \alpha\eta\frac{\partial\eta}{\partial x} = \frac{\beta c_0}{2H}\frac{\partial^2}{\partial x^2}\int_{-\infty}^{+\infty}\eta(x',t) \times\left[\coth\frac{\pi(x-x')}{2H} - \mathrm{sgn}(x-x')\right]dx', \quad (1)$$

where α and β are environmental parameters, and given by

$$\alpha = \frac{3c_0\int_{-H}^{0}\left(\frac{\partial\phi}{\partial z}\right)^3 dz}{2\int_{-H}^{0}\left(\frac{\partial\phi}{\partial z}\right)^2 dz}, \quad (2)$$

$$\beta = \frac{1}{2\int_{z_0}^{0}\left(\frac{\partial\phi}{\partial z}\right)^2 dz}. \quad (3)$$

Table 1. Soliton Wavelengths

Wavelength	λ_{12}	λ_{23}	λ_{34}	λ_{45}	$\bar{\lambda}$ (mean)
Value, km	1.1	1.2	0.8	0.6	0.9

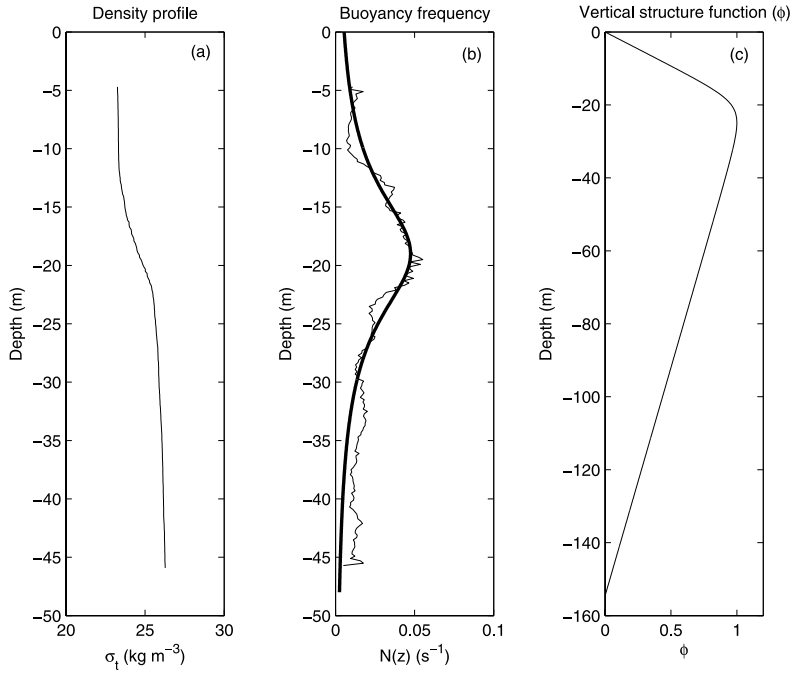

Figure 4. (a) The background density profile, (b) the buoyancy frequency, and (c) the vertical structure function for water depth 154.6 m. The thick line in Figure 4b shows the three-parameter buoyancy frequency model, which is best fitted to the measured data.

The steady solution to equation (1) has the form [*Joseph*, 1977; *Zheng et al.*, 1993]

$$\eta(\xi; a, b) = \frac{-\eta_0}{\cosh^2 a\xi + \left(\sinh^2 a\xi\right)/(a^2b^2)}, \tag{4}$$

where a is a wave number-like parameter satisfying the relationship

$$ab\tan(aH) = 1, \tag{5}$$

and

$$b = -\frac{4\beta c_0}{\alpha\eta_0}. \tag{6}$$

The nonlinear soliton phase speed is written as

$$c = c_0\left[1 + \frac{\beta}{H}(1 - \delta\cot\delta)\right], \tag{7}$$

where $\delta = 2aH$. The horizontal velocity is given by

$$u = -\frac{c_0\eta_0}{\cosh^2 a\xi + \left(\sinh^2 a\xi\right)/(a^2b^2)}\frac{\partial\phi}{\partial z}. \tag{8}$$

[10] Using equation (A7), we derive the soliton-induced normalized radar backscatter cross section per unit area ($\hat{\sigma}_{0\mathrm{IS}}$)

$$\hat{\sigma}_{0\mathrm{IS}} = \frac{1}{M}\frac{\sinh 2a\xi}{\left(\cosh^2 a\xi + \frac{1}{a^2b^2}\sinh^2 a\xi\right)^2}, \tag{9}$$

where M is the maximum value of the function $\sinh 2a\xi/\left(\cosh^2 a\xi + \frac{1}{a^2b^2}\sinh^2 a\xi\right)^2$.

4. Dynamic Interpretation of the Internal Solitons

4.1. Vertical Structure

[11] The background density profiles were sampled by a Seabird CTD on a towed TRIAXUS vehicle during the RISE project cruise in July 2004. A typical density profile in the area where the internal waves are observed (Figure 4a) was derived based on the data collected on 20 July 2004 at 01:30:00 UTC. The buoyancy frequency is calculated and shown in Figure 4b. In order to obtain an analytical solution to the vertical structure equation under the continuous stratification condition, we use a three-parameter function to represent the buoyancy frequency, as suggested by *Vlasenko* [1994],

$$N(z) = \frac{N_{\mathrm{m}}}{C_1(z/H + C_2)^2 + 1}, \tag{10}$$

where N_{m} is maximum of N; $C_1 = (2H/\delta h)^2$, and $C_2 = h/H$; h is the pycnocline depth; δh is the width of N at half N_{m} and is regarded as the pycnocline thickness. This three-parameter function provides a realistic model of the oceanic pycnocline in the area where the solitons were observed. The three-parameter buoyancy frequency model is also shown in Figure 4b in a thick curve, which is best fitted to the derived buoyancy frequency data and in which parameters h, δh, and N_{m} are taken as 19.0 m, 13.7 m, and 0.047 s^{-1}, respectively.

[12] Observations showed that in the Columbia River mouth region, internal solitons have the most energy at

their first modes [*Nash and Moum*, 2005]. For this buoyancy frequency model, the vertical structure equation has an analytic solution at the first mode [*Vlasenko*, 1994]

$$\phi(z) = \phi_0 \sqrt{C_1\left(\frac{z}{H} + C_2\right)^2 + 1}\,\sin(\pi z_*), \tag{11}$$

and

$$c_0 = \frac{HN_{\mathrm{m}}}{\pi^2/\Gamma^2 - C_1}, \tag{12}$$

in which

$$z_* = \frac{\arctan\sqrt{C_1}(z/H + C_2) - \arctan\sqrt{C_1}C_2}{\sqrt{C_1}\Gamma}, \tag{13}$$

and

$$\Gamma = \frac{\arctan\sqrt{C_1}(C_2 - 1) - \arctan\sqrt{C_1}C_2}{\sqrt{C_1}}. \tag{14}$$

[13] Using equations (11), (12), (13), and (14), we calculate the soliton vertical structure function for soliton S1, which is shown in Figure 4c. The first-mode linear wave speed c_0 is 0.58 m s^{-1}.

4.2. Characteristic Half-Width

[14] Here we define the soliton characteristic half-width, D_{half}, as a horizontal distance over which the soliton amplitude decreases from its peak value to half the peak value, and, therefore,

$$D_{half} = \frac{2}{a}\,\mathrm{asinh}\left[\frac{1}{\sqrt{1 + \tan^2 aH}}\right]. \tag{15}$$

Substituting $b = 1/a\,\tan(aH)$ into equation (9) yields

$$\hat{\sigma}_{0\mathrm{IS}} = \frac{1}{M}\,\frac{\sinh 2a\xi}{\left(\cosh^2 a\xi + \tan^2 aH \sinh^2 a\xi\right)^2}. \tag{16}$$

[15] One can see that the parameter a must be determined to estimate dynamic parameters of an internal soliton. In practice, equation (16) is modified to

$$I_0 = \frac{A \sinh 2a(\xi - \xi_0)}{\left[\cosh^2 a(\xi - \xi_0) + \tan^2 aH \sinh^2 a(\xi - \xi_0)\right]^2} + B, \tag{17}$$

where I_0 represents the SAR image intensity value. There are four parameters (A, a, ξ_0, and B) in equation (17). To determine these parameters, we use a nonlinear least squares method, which generates the best fit between equation (17) and the SAR image intensity data. Figures 5a–5e show the SAR soliton image intensity values and the nonlinear least squares-solved theoretical I_0 for solitons S1, S2, S3, S4, and S5, respectively. The soliton characteristic half-width can then be calculated by equation (15) from the derived parameter a. For soliton S1, the parameter a is 7.2×10^{-3} m^{-1}, and the water depth is 154.6 m, so the characteristic half-width is calculated as 119.3 m. In same manner, the characteristic half-widths of S2, S3, S4, and S5 are obtained and listed in Table 2.

4.3. Amplitude, Phase Speed, and Velocities

[16] From equations (5) and (6), we derive the soliton amplitude

$$\eta_0 = -\frac{4\beta c_0}{\alpha}\,a\tan(aH). \tag{18}$$

For S1, $\alpha = -0.038$ s^{-1}, $\beta = 10.43$ m, and $H = 154.6$ m. The amplitude η_0 is

$$\eta_0 = 9.3 \text{ m}. \tag{19}$$

Using equation (7), we calculate the soliton phase speed

$$c = 0.69 \text{ m s}^{-1}. \tag{20}$$

[17] The maximum horizontal water particle velocity is at $\xi = 0$, derived from equation (8)

$$u = -c_0\eta_0\phi_z. \tag{21}$$

The average upper- (from z_0 to 0) and lower-layer (from $-H$ to z_0) horizontal velocities are written as

$$U_1 = \frac{1}{|z_0|}\int_{z_0}^{0} -c_0\eta_0\phi_z dz = \frac{c_0\eta_0}{|z_0|}, \tag{22}$$

and

$$U_2 = \frac{1}{H - |z_0|}\int_{-H}^{z_0} -c_0\eta_0\phi_z dz = -\frac{c_0\eta_0}{H - |z_0|}. \tag{23}$$

For S1, the average upper- and lower-layer velocities are

$$U_1 = 0.22 \text{ m s}^{-1} \quad \text{and} \quad U_2 = -0.04 \text{ m s}^{-1}. \tag{24}$$

Results for all waves along section A-A′ are given in Table 2.

4.4. Energy Flux

[18] The average energy per unit crest length for an internal soliton is [*Phillips*, 1977; *Zheng et al.*, 1993, 1995]

$$E = \delta\rho g\overline{\eta^2}, \tag{25}$$

where

$$\begin{aligned}\overline{\eta^2} &= \frac{1}{2D_{half}}\int_{-D_{half}}^{D_{half}} \eta^2(x,t)\mathrm{d}x \\ &= \frac{\eta_0^2}{2D_{half}}\int_{-D_{half}}^{D_{half}} \left[\frac{1}{\cosh^2 a(x - ct) + \sinh^2 a(x - ct)/(a^2b^2)}\right]^2 dx.\end{aligned} \tag{26}$$

$\delta\rho$ represents the density difference between upper and lower layers and is approximated by $\int_{-h-\delta h}^{-h+\delta h}\frac{\rho_0}{g}[N(z)]^2 dz$,

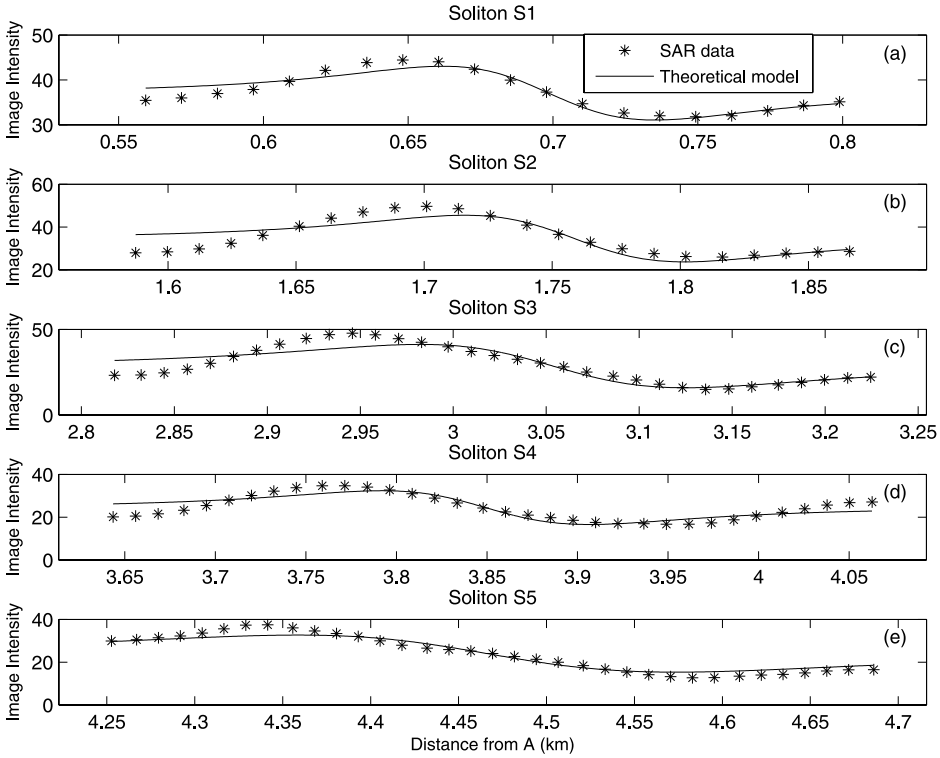

Figure 5. The SAR image intensity value (asterisks) and the theoretical radar backscatter model (solid line) computed by the nonlinear least squares curve fitting for (a) S1, (b) S2, (c) S3, (d) S4, and (e) S5.

where ρ_0 is the average density. For a single soliton, *Zheng et al.* [1993, 1995] demonstrated that the group speed (c_g) equals to the phase speed, namely, $c_g = c$. Therefore, with $t = 0$, the average energy flux (F) for unit wave crest length of an internal soliton is

$$F = Ec_g = \frac{\delta \rho g \eta_0^2 c}{2D_{half}} \int_{-D_{half}}^{D_{half}} \left[\frac{1}{\cosh^2 ax + \sinh^2 ax/(a^2 b^2)} \right]^2 dx. \tag{27}$$

For solitons S1, S2, S3, S4, and S5, the average energy fluxes per unit crest length are 417.4, 294.1, 97.2, 167.0, and 39.7 W m^{-1}, respectively.

5. Discussion

5.1. The Influence of the SAR Beam Angle

[19] Our analysis method is based on the fact that the SAR radar backscatter cross section per unit area is proportional to the surface velocity convergence caused by an internal soliton velocity field. The radar backscatter cross section, however, is related to the SAR beam look angle relative to the soliton wave direction; the radar backscattering weakens if the angle increases, as shown by equation (A7). Fortunately, this angle-dependent relationship cannot affect the SAR image interpretation results. Along a section across the internal solitons, the angle effect is uniform, and the radar backscatter cross section is normalized in equation (9). The normalization removes the term in equation (A7) containing the SAR beam looking angle (χ). This process actually eliminates the influence of the look angle on the radar backscatter cross section in deriving the soliton parameters if the SAR radar backscattering is strong enough. However, as the look angle increases to 90°, the backscatter signal decreases and the internal solitons eventually become undetectable.

5.2. Relationship of Velocity Divergence to Soliton Parameters

[20] Equation (9) shows that only the normalized velocity divergence is used to derive the soliton dynamic parameters. The normalized form of the divergence is given by

$$\frac{\overline{du}}{dx} = -\frac{1}{M} \frac{\sinh 2ax}{(\cosh^2 ax + \tan^2 aH \sinh^2 ax)^2}. \tag{28}$$

[21] Based on equation (28), we investigate the dependence of the normalized du/dx for S1 on D_{half}, η_0, and c.

Table 2. Internal Soliton Dynamic Parameters

Soliton (Sec AA′)	D_{half}, m	c_0, m s^{-1}	η_0, m	c, m s^{-1}	U_1, m s^{-1}	U_2, m s^{-1}	F, W m^{-1}	H, m
S1	119.3 (±14.7)	0.58 (±0.07)	9.3 (±2.6)	0.69 (±0.10)	0.22 (±0.07)	0.04 (±0.02)	417.4 (±281.6)	154.6
S2	141.1 (±25.9)	0.60 (±0.07)	7.8 (±2.7)	0.69 (±0.10)	0.19 (±0.07)	0.03 (±0.01)	294.1 (±242.4)	205.4
S3	231.7 (±38.1)	0.61 (±0.07)	4.5 (±1.5)	0.67 (±0.09)	0.11 (±0.04)	0.01 (±0.005)	97.2 (±70.3)	285.8
S4	190.2 (±33.3)	0.61 (±0.07)	5.9 (±2.0)	0.68 (±0.09)	0.15 (±0.05)	0.01 (±0.006)	167.0 (±120.1)	312.8
S5	342.0 (±44.3)	0.61 (±0.07)	3.0 (±0.9)	0.65 (±0.09)	0.07 (±0.02)	0.01 (±0.002)	39.7 (±24.3)	347.4

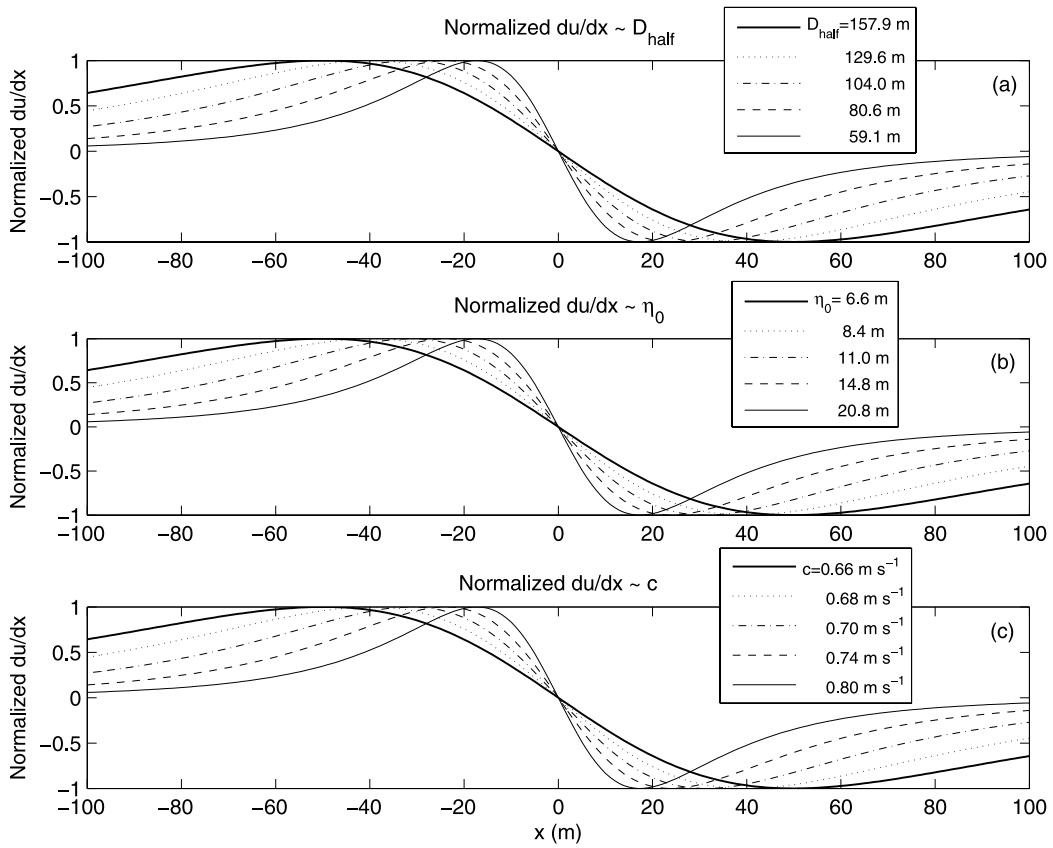

Figure 6. The normalized soliton-induced velocity divergence ($\overline{\frac{du}{dx}}$) versus distance (x) in different soliton (a) half-width, (b) amplitude, and (c) phase speed.

Results are shown in Figure 6. One can see that the normalized velocity divergence curves display variations with the half-width varying from 157.9 to 59.1 m (Figure 6a), η_0 from 6.6 to 20.8 m, and c from 0.66 to 0.80 m s^{-1}. The curve patterns of the normalized divergence exhibit obvious, monotonic changes. Clearly, the normalized du/dx is sensitive to soliton parameter, and it is appropriate to derive soliton parameters from $\overline{du/dx}$.

5.3. Sensitivity to Stratification

[22] The derived soliton dynamic parameters are related to the background density profile, and therefore departure of an assumed density profile from the actual ambient stratification influences the SAR image interpretation. Variations in the stratification can alter ϕ, c_0, α, and β, and these parameters cause changes in amplitude, soliton phase speed, and water velocities. Because of the complex, nonlinear relationships between the soliton dynamic parameters and the ambient stratification, the sensitivities of the amplitude, phase speed, and velocities to variations in the stratification parameters are estimated numerically for a particular soliton (S1).

[23] Figure 7 shows the soliton parameter variations corresponding to the changes in the pycnocline depth h. Figure 7a reveals that D_{half} is independent of h. However, η_0, c_0, c, and U_2 increase with h (Figures 7b–7d and 7f), while Figure 7e suggests that U_1 is inversely proportional to h. Figure 8 shows changes in the soliton parameters D_{half}, η_0, c_0, c, U_1, and U_2 with the pycnocline thickness δh. The D_{half} is not affected by δh (Figure 8a). Figures 8b–8f indicate that η_0, c_0, c, and U_2 increase with δh, but U_1 decreases with δh. The effects of the maximum buoyancy frequency N_m on the estimates of the soliton parameters are shown in Figure 9. Like Figures 7a and 8a, Figure 9a reveals that D_{half} is not related to N_m. In addition, Figure 9b suggests that η_0 is not influenced by N_m, while the parameters c_0, c, and U_2 increase linearly with N_m. Table 3 lists the average change rates of D_{half}, η_0, c_0, c, U_1, and U_2 with respect to h, δh, and N_m.

[24] To summarize the significance of Figures 7, 8, and 9 and Table 3, we see that the soliton half-width D_{half} is not affected by the assumed stratification. D_{half} is calculated using the parameter a, which is obtained from the SAR image. The stratification information is not needed in the half-width calculation because the SAR image directly contains sufficient information in horizontal dimension regarding the soliton. Also, the pycnocline thickness has less influence on the soliton amplitude and upper- and lower-layer velocities than the pycnocline depth. The pycnocline depth and thickness have almost same effects on the linear wave speed and soliton phase speed.

5.4. Uncertainty Analysis

[25] The soliton half-width is calculated from the parameter a. In order to analyze the uncertainty of the soliton parameters, we need first to estimate the uncertainty of the

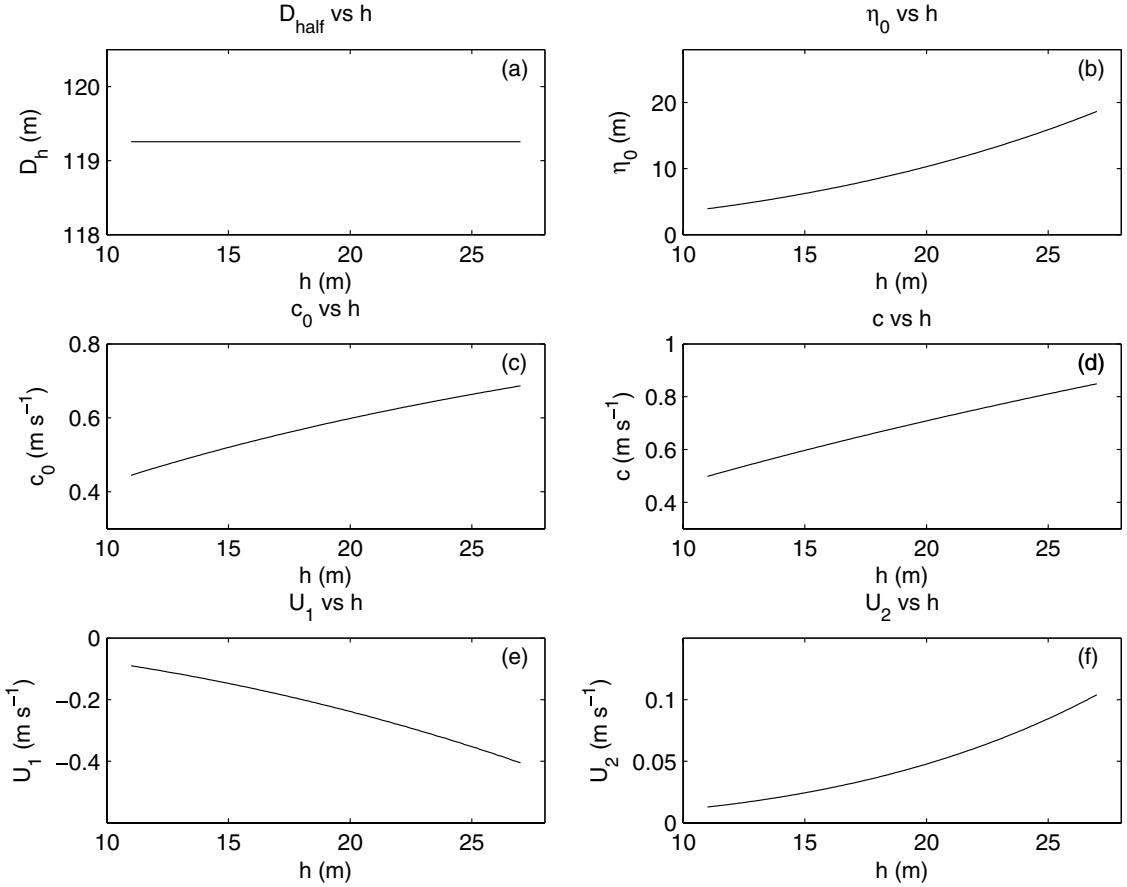

Figure 7. The sensitivities of the derived soliton parameters (a) half-width, (b) amplitude, (c) linear wave speed, (d) soliton phase speed, (e) upper-layer average velocity, and (f) lower-layer average velocity to the stratification parameter pycnocline depth.

parameter a. From equation (17), the SAR image intensity value can be rewritten as

$$I_0 = I_0(a, A, B, \xi_0, x), \tag{29}$$

and a group of SAR image intensity values is

$$I_0^{\mathrm{o}} = \left[I_{01}^{\mathrm{o}}, I_{02}^{\mathrm{o}}, I_{03}^{\mathrm{o}}, \ldots, I_{0n}^{\mathrm{o}}\right] \quad \text{at} \quad x = [x_1, x_2, x_3, \ldots, x_n]. \tag{30}$$

[26] Let a_m, A_m, B_m, and ξ_{0m} be the optimal estimates of the parameters a, A, B, and ξ_0, respectively, and, therefore, the RMS deviation of I_0 between the observations and theoretical model is [*Townend*, 2002]

$$Dev = \sqrt{\frac{1}{n}\sum_{i=1}^{n}\left[I_{0i}^{\mathrm{o}} - I_0(a_m, A_m, B_m, \xi_{0m}, x_i)\right]^2}. \tag{31}$$

[27] The RMS deviation (Dev_1) of I_0 caused by the uncertainty of a is written as

$$\mathrm{Dev}_1 = \sqrt{\overline{\left(\frac{\partial I_0}{\partial a}\right)^2}}\,\Delta a. \tag{32}$$

The total Dev is the sum of uncertainties produced by the four parameters. In order to give a reasonable estimate of Dev_1, we assume $Dev_1 = Dev/4$. The uncertainty of the parameter a is obtained as

$$\Delta a = \frac{Dev}{4\sqrt{\overline{\left(\frac{\partial I_0}{\partial a}\right)^2}}}. \tag{33}$$

The uncertainty of D_{half}, which can be derived from equation (15), is

$$\Delta D_{half} = \left|\left\{-\frac{2}{a^2}a\sinh\left[\frac{1}{\sqrt{1+\tan^2 aH}}\right] - \frac{2H\tan aH\sec^2 aH}{\sqrt{1+\tan^2 aH}(2+\tan^2 aH)}\right\}\right||\Delta a|, \tag{34}$$

[28] The η_0, c, U_1, U_2, and F are the functions of the parameter a and stratification parameters h, δh, and N_{m}

$$\tau = T(a, h, \delta h, N_m), \tag{35}$$

where τ can be c, c_0, D_{half}, η_0, U_1, U_2, or F. T is defined by equations (7), (12), (15), (18), (22), (23), and (27) for c, c_0, D_{half}, η_0, U_1, U_2, and F, respectively. The uncertainty is given by

$$\Delta\tau \le \left|\frac{\partial \mathrm{T}}{\partial a}\right||\Delta a| + \left|\frac{\partial \mathrm{T}}{\partial h}\right||\Delta h| + \left|\frac{\partial \mathrm{T}}{\partial \delta h}\right||\Delta \delta h| + \left|\frac{\partial \mathrm{T}}{\partial N_{\mathrm{m}}}\right||\Delta N_{\mathrm{m}}|. \tag{36}$$

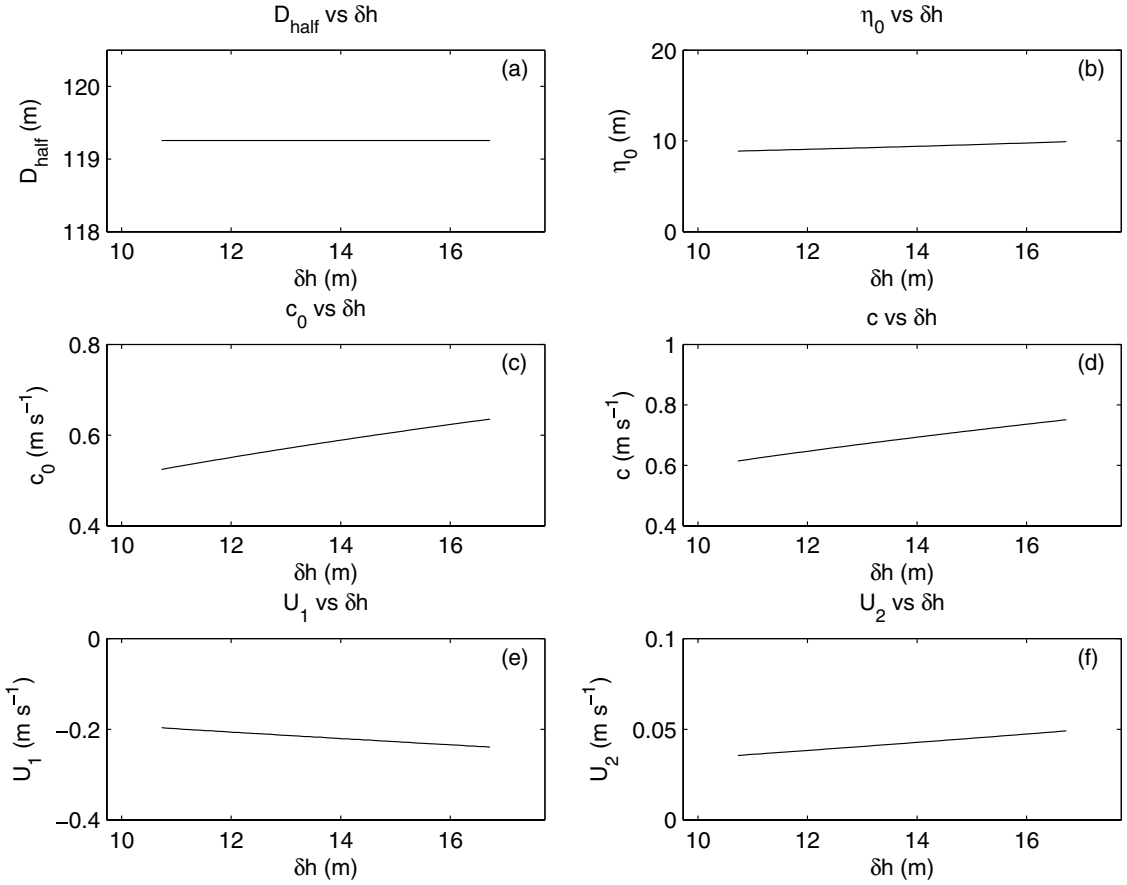

Figure 8. The sensitivities of the derived soliton parameters (a) half-width, (b) amplitude, (c) linear wave speed, (d) soliton phase speed, (e) upper-layer average velocity, (f) and lower-layer average velocity to the stratification parameter pycnocline thickness.

[29] Assume that h, δh, and N_{m} have uncertainties of 5, 10, and 5%, respectively, which correspond to a 28% uncertainty in the stratification model above 50 m depth. Using equation (36), we calculate the uncertainties for c, c_0, D_{half}, η_0, U_1, U_2, and F. The results are listed in Table 2 with parentheses.

[30] In order to examine the error ranges of the soliton parameters, we choose additional five sections across the leading soliton shown in Figure 1. These sections are marked by 1, 2, 3, 4, and 5 from south to north. Table 4 lists the derived soliton parameters, their means, and the standard deviations (STD) of the leading soliton parameters along the five sections. The differences between the means of the leading soliton parameters along the five sections and the previously derived soliton parameters for S1 are also listed in Table 4. The standard deviations of D_{half}, η_0, and c are 10, 12, 2% of their means, respectively. These deviations are within the error ranges derived above.

6. Summary

[31] In this study, we analyze a SAR image displaying a group of internal solitons generated at the Columbia River plume front and traveling offshore from that front. We have developed a theoretical model of the radar backscatter cross section for finite-depth internal solitons in a continuously stratified medium, which specifies the relationship between the SAR image intensity and the dynamic parameters of the internal soliton. A three-parameter stratification model is used to simulate real ocean stratification. The three parameters are the pycnocline depth, thickness, and maximum buoyancy frequency, which are obtained from in situ data. Using the theoretical radar backscatter cross-section model and the stratification parameters, we interpret the SAR image and derive the internal soliton dynamic parameters of half-width, amplitude, phase speed, water particle velocities, and energy flux by fitting the theoretical model to the SAR image data. The sensitivities of the derived soliton parameters to the stratification are analyzed, indicating that the estimated amplitude is less affected by the pycnocline thickness than the pycnocline depth. The soliton half-width can be obtained without the stratification information.

Appendix A: SAR Imaging of Internal Solitons

[32] Under the equilibrium and steady condition, the high-frequency capillary-gravity wave spectrum (Ψ) can be written as [*Yuan*, 1997; *Zheng et al.*, 2001; 2004]

$$\Psi = m_3^{-1}\left[m\left(\frac{u*}{c_{sw}}\right)^2 - 4\gamma^2 k_{sw}^2 \varpi^{-1} - S_{\alpha\beta}\frac{\partial U_\beta}{\partial x_\alpha}\omega^{-1}\right]k_{sw}^{-4}, \quad \text{(A1)}$$

where m_3 and m are coefficients; u_* is the friction wind speed; ϖ, k_{sw}, and c_{sw} are the angular frequency, the wave

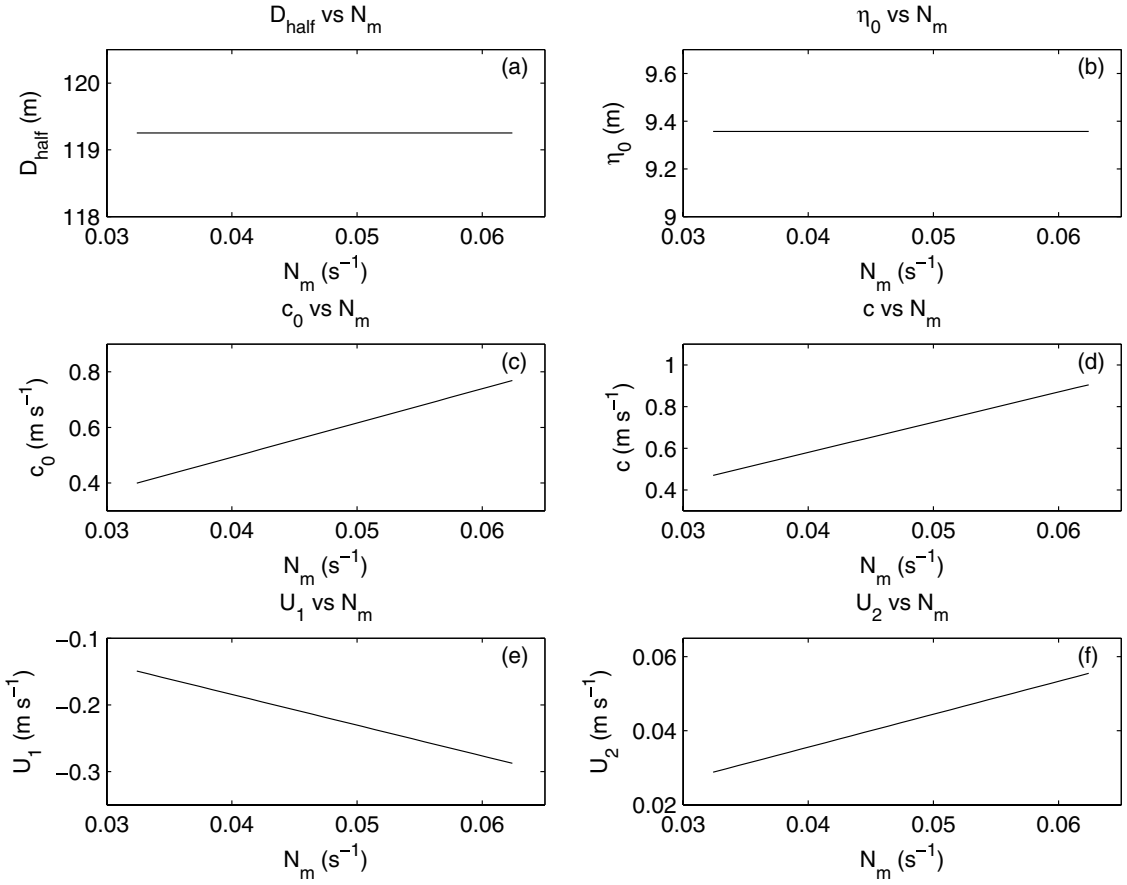

Figure 9. The sensitivities of the derived soliton parameters (a) half-width, (b) amplitude, (c) linear wave speed, (d) soliton phase speed, (e) upper-layer average velocity, and (f) lower-layer average velocity to the stratification parameter maximum buoyancy frequency.

number, and phase speed of surface waves, respectively; and γ represents the viscosity. U_β denotes the velocity components of the large-scale current field, and $S_{\alpha\beta}$ represents the excess momentum flux tensor. Subscripts α and β represent the horizontal coordinates (x or y). Thus

$$S_{\alpha\beta}\frac{\partial U_\alpha}{\partial x_\beta}=\frac{1}{2}\left[\frac{\partial u}{\partial x}\cos^2\varphi+\left(\frac{\partial u}{\partial y}+\frac{\partial v}{\partial x}\right)\cos\varphi\sin\varphi+\frac{\partial v}{\partial y}\sin^2\varphi\right], \tag{A2}$$

where φ is the wave direction. For the ocean surface, the radar backscatter cross section per unit area, σ_0, is given by [*Plant*, 1990]

$$\sigma_0(\theta)_{ij}=16\pi k_0^2\left|g_{ij}(\theta)\right|^2\Psi(0,2k_0\sin\theta), \tag{A3}$$

where θ and k_0 represent the incidence angle and wave number of radar waves, respectively; Ψ is the two-dimensional wave number spectral density of the ocean surface waves satisfying the Bragg resonant scatter condition; the indices i and j denote the polarizations of the incident and backscattered radiations, respectively; and $g_{ij}(\theta)$ are the first-order scattering coefficients. Under horizontal and vertical polarization conditions, g_{ij} is written as

$$g_{HH}(\theta)=\frac{(\varepsilon_r-1)\cos^2\theta}{\left[\cos\theta+\left(\varepsilon_r-\sin^2\theta\right)^{1/2}\right]^2}, \tag{A4}$$

and

$$g_{VV}(\theta)=\frac{(\varepsilon_r-1)\left[\varepsilon_r\left(1-\sin^2\theta\right)-\sin^2\theta\right]\cos^2\theta}{\left[\varepsilon_r\cos\theta+\left(\varepsilon_r-\sin^2\theta\right)^{1/2}\right]^2}, \tag{A5}$$

respectively, where ε_r is the relative dielectric constant of seawater [*Saxton and Lane*, 1952; *Klein and Swift*, 1977]. Therefore we have

$$\sigma_0(\theta)_{ij}=16\pi k_0^2\left|g_{ij}(\theta)\right|^2 m_3^{-1}\cdot\left[m\left(\frac{u*}{c_{sw}}\right)^2-4\gamma^2k_{sw}^2\varpi^{-1}-S_{\alpha\beta}\frac{\partial U_\beta}{\partial x_\alpha}\omega^{-1}\right]k_{sw}^{-4}, \tag{A6}$$

Table 3. Average Change Rates of the Dynamic Parameters With h, δh, and N_m

ΔP	ΔD_{half}	$\Delta\eta_0$	Δc_0	Δc	ΔU_1	ΔU_2
$\Delta P/\Delta h$	0, m/m	0.9, m/s	0.015, m s^{-1}/m	0.02, m s^{-1}/m	−0.02, m s^{-1}/m	0.006, m s^{-1}/m
$\Delta P/\Delta\delta h$	0, m/m	0.2, m/s	0.02, m s^{-1}/m	0.02, m s^{-1}/m	−0.007, m s^{-1}/m	0.002, m s^{-1}/m
$\Delta P/\Delta N_m$	0, m/10^{-2} s^{-1}	0, m/10^{-2} s^{-1}	0.12, m s^{-1}/10^{-2} s^{-1}	0.15, m s^{-1}/10^{-2} s^{-1}	−0.05, m s^{-1}/10^{-2} s^{-1}	0.05, m s^{-1}/10^{-2} s^{-1}

Table 4. Dynamic Parameters for the Leading Soliton

Soliton	D_{half}, m	c_0, m s^{-1}	η_0, m	c, m s^{-1}	U_1, m s^{-1}	U_2, m s^{-1}	F, W m^{-1}	H, m
Sec 1	102.9	0.59	11.2	0.71	0.26	0.05	627.5	164.1
Sec 2	109.4	0.58	10.4	0.69	0.24	0.05	526.9	144.6
Sec 3	129.6	0.58	8.4	0.67	0.19	0.04	334.4	136.2
Sec 4	123.9	0.57	9.0	0.67	0.21	0.05	379.6	131.3
Sec 5	99.4	0.58	11.7	0.70	0.27	0.06	677.9	132.7
Mean	113.1	0.58	10.2	0.69	0.24	0.05	509.3	
STD	11.8	0.005	1.3	0.016	0.03	0.007	134.2	
|Mean-S1|	6.2	0.00	0.9	0.00	0.02	0.01	91.9	

where $k_{sw} = 2k_0\sin\theta$. The first two terms of the right-hand side of equation (A6) represent wind inputs and viscosity dissipation, respectively. On the horizontal scale of an internal wave packet, these terms are supposed to be uniform, so they only contribute to the background of an internal wave SAR image [*Zheng et al.*, 2001]. The third term reflects effects of the internal wave. Considering two-dimensional (x, z) internal waves with x in the internal wave propagation direction, we have $\varphi = 0$, and therefore the second and third terms of equation (A2) vanish. Thus, taking into account the SAR beam looking angle (χ) relative to the wave direction, the soliton-induced radar backscatter cross section per unit area, $\sigma_{0\mathrm{IS}}(\theta)_{\mathrm{ij}}$, is written as

$$\sigma_{0IS}(\theta)_{ij} = 8\pi k_0^2 m_3^{-1} \left|g_{ij}(\theta)\right|^2 \cos\chi k_{sw}^{-4}\left[-\frac{\partial(u|_{z=0})}{\partial x}\right]. \qquad \text{(A7)}$$

[33] **Acknowledgments.** This study is supported by the National Science Foundation RISE Project OCE 0239072 and is RISE contribution #10. We thank Captain Ron L. Short of the R/V Pt Sur and marine technicians Stewart Lamberdin and Ben Jokinen for their superb support in in situ data collection. The SAR image was provided by Comprehensive Large Array-data Stewardship System (CLASS) of National Oceanic and Atmospheric Administration (NOAA). The authors are also grateful to the anonymous reviewers for their valuable suggestions and comments.

References

Apel, J. R., and F. I. Gonzalez (1983), Nonlinear features of internal waves off Baja California as observed from the Seasat imaging radar, *J. Geophys. Res.*, *88*, 4459–4466.

Apel, J. R., J. R. Holbrook, A. K. Liu, and J. J. Tsai (1985), The Sulu Sea internal soliton experiment, *J. Phys. Oceanogr.*, *15*, 1625–1651.

Benjamin, T. B. (1966), Internal waves of finite amplitude and permanent form, *J. Fluid Mech.*, *25*, 241–271.

Benjamin, T. B. (1967), Internal waves of permanent form in fluids of great depth, *J. Fluid Mech.*, *29*, 559–592.

Benney, D. J. (1966), Long non-linear waves in fluids, *J. Math Phys.*, *45*, 52–63.

Fu, L.-L., and B. Holt (1984), Internal waves in the Gulf California: Observation from a space-borne radar, *J. Geophys. Res.*, *89*, 2053–2060.

Joseph, R. I. (1977), Solitary waves in a finite depth fluid, *J. Phys. A Math. Gen.*, *10*, L1225–L1227.

Klein, L. A., and C. T. Swift (1977), An improved model for the dielectric constant of sea water at microwave frequencies, *IEEE Trans. Antennas Propag.*, *25*, 105–111.

Kubota, T., D. R. Ko, and L. Dobbs (1978), Propagation of weakly nonlinear internal waves in a stratified fluid of finite depth, *J. Hydronaut.*, *12*, 157–165.

Liu, A. K., J. R. Holbrook, and J. R. Apel (1985), Nonlinear internal wave evolution in the Sulu Sea, *J. Phys. Oceanogr.*, *15*, 1613–1624.

Liu, A. K., Y. S. Chang, M.-K. Hsu, and N. K. Liang (1998), Evolution of nonlinear internal waves in the East and South China Seas, *J. Geophys. Res.*, *103*, 7995–8008.

Moum, J. N., D. M. Farmer, W. D. Smyth, L. Armi, and S. Vagle (2003), Structure and generation of turbulence at interfaces strained by internal solitary waves propagating shoreward over the continental shelf, *J. Phys. Oceanogr.*, *33*, 2093–2112.

Nash, J. D., and J. N. Moum (2005), River plumes as a source of large-amplitude internal waves in the coastal ocean, *Nature*, *437*, 400–403, doi:10.1038/nature03936.

Ono, H. (1975), Algebraic solitary waves in stratified fluid, *J. Phys. Soc. Jpn.*, *39*, 1082–1091.

Orton, P. M., and D. A. Jay (2005), Observations at the tidal plume front of a high-volume river outflow, *Geophys. Res. Lett.*, *32*, L11605, doi:10.1029/2005GL022372.

Osborn, A. R., and T. L. Burch (1980), Internal solitons in the Andaman Sea, *Science*, *208*, 451–460.

Phillips, O. M. (1977), *The Dynamic of the Upper Ocean*, 2nd ed., 336 pp., Cambridge Univ. Press, New York.

Plant, W. J. (1990), Bragg scattering of electromagnetic waves from the air/sea interface, in *Surface Waves and Fluxes, Vol. II: Remote Sensing*, edited by G. L. Geemaet and W. J. Plant, pp. 41–168, Springer New York.

Saxton, J. A., and J. A. Lane (1952), Electrical properties of sea water, *Wirel. Eng.*, *291*, 269–275.

Stanton, T. P., and L. A. Ostrovsky (1998), Observations of highly nonlinear internal solitons over the continental shelf, *Geophys. Res. Lett.*, *25*, 2695–2698.

Townend, J. (2002), *Practical Statistics for Environmental and Biological Scientists*, 276 pp., John Wiley, Hoboken, N. J.

Vlasenko, V. I. (1994), Multimodal soliton of internal waves, *Izv. Atmos. Ocean. Phys.*, *30*, 161–169.

Yuan, Y. (1997), Representation of high frequency spectra of ocean waves and the basis for analyzing SAR images, *Chin. J. Oceanol. Limnol.*, *28*, 1–5.

Zheng, Q., X.-H. Yan, and V. Klemas (1993), Statistical and dynamical analysis of internal waves on the continental shelf of Middle Atlantic Bight from space shuttle photographs, *J. Geophys. Res.*, *98*, 8495–8504.

Zheng, Q., V. Klemas, and X.-H. Yan (1995), Dynamic interpretation of space shuttle photographs: Deepwater internal waves in the western equatorial Indian Ocean, *J. Geophys. Res.*, *100*, 2579–2590.

Zheng, Q., Y. Yuan, V. Klemas, and X.-H. Yan (2001), Theoretical expression for an ocean internal soliton synthetic aperture radar image and determination of the soliton characteristic half width, *J. Geophys. Res.*, *106*, 31,415–31,424.

Zheng, Q., P. Clemente-Colón, X.-H. Yan, W. T. Liu, and N. E. Huang (2004), Satellite synthetic aperture radar detection of Delaware Bay plumes: Jet-like feature analysis, *J. Geophys. Res.*, *109*, C03031, doi:10.1029/2003JC002100.

D. A. Jay and J. Pan, Department of Civil and Environmental Engineering, Portland State University, Portland, Oregon 97201, USA. (djax@cecs.pdx.edu; panj@cecs.pdx.edu)

P. M. Orton, Lamont-Doherty Earth Observatory, Columbia University, Palisades, NY 10964, USA. (orton@ldeo.columbia.edu)